Structural Monitoring and Maintenance, *Vol. 4, No. 3 (2017) 269-299*
DOI: https:// doi.org/10.12989/smm.2017.4.3.269

Nondestructive damage evaluation of deep beams

Selcuk Dincal*[1] and Norris Stubbs[2a]

[1]2H Offshore Inc., 15990 North Barkers Landing, Suite 200, Houston, TX 77079, USA
[2]Zachry Department of Civil Engineering, Texas A&M University, 3136 TAMU, College Station, TX 77843, USA

(Received August 8, 2017, Revised August 30, 2017, Accepted September 2, 2017)

Abstract. This paper presents a Level III damage evaluation methodology, which simultaneously, identifies the location, the extent, and the severity of stiffness damage in deep beams. Deep beams are structural elements with relatively high aspect (depth-to-length) ratios whose response are no longer based on the simplified Euler-Bernoulli theory. The proposed methodology is developed on the bases of the force-displacement relations of the Timoshenko beam theory and the concept of invariant stress resultants, which states that the net internal force existing at any cross-section of the beam is not affected by the inflicted damage, provided that the external loadings in the undamaged and damaged beams are identical. Irrespective of the aspect ratios, local changes in both the flexural and the shear stiffnesses of beam-type structures may be detected using the approach presented in this paper.

Keywords: nondestructive damage evaluation; deep beams; Timoshenko beam theory; stress resultants; modal flexibility

1. Introduction

Vibration-based nondestructive damage evaluation (NDE) relates changes in to the physical properties of a structural system to the system's response characteristics. Vibration-based NDE offers global damage evaluation methodologies that are well suited for continuous health monitoring of structural systems. Rytter (1993) categorized NDE methodologies into four classes on the basis of the end information provided: (1) Level I: Detection of the damage; (2) Level II: Localization of the damage; (3) Level III: Assessment of the severity of the damage; and (4) Level IV: Performance evaluation of the structure after the Level III assessment. To date, most NDE methodologies are limited to damage detection and localization only (i.e., Level I and Level II). For example, Lifshitz and Rotem (1969) utilized the changes in peak frequencies to detect the presence of damage (i.e., a Level I method). Cawley and Adams (1979) presented a Level II damage evaluation methodology that utilized the ratio of the frequency changes to localize damage in two-dimensional structures. Several Level II methodologies followed the pioneering work of Cawley and Adams (Pandey *et al.* 1991, Pandey and Biswas (1994), Zhang and Aktan (1995), Zimmerman and Kaouk (1994), Stubbs *et al.* 1992, Choi *et al.* 2005). Research performed by Hjelmstad and Shin (1996), Stubbs and Kim (1996, 2002, 2003), and Choi *et al.* 2005 may be listed amongst the significant Level III NDE

---

*Corresponding author, Ph.D., E-mail: selcukdincal@gmail.com
[a] Professor

http://www.techno-press.org/?journal=smm&subpage=7 ISSN: 2288-6605 (Print), 2288-6613 (Online)

methodologies proposed to date.

Upon reviewing the body of global NDE algorithms proposed so far, several shortcomings may be listed: (1) Most proposed NDE methodologies are ad-hoc and are not based on the fundamental principles of mechanics (e.g., equilibrium, stress-strain, compatibility, the principle of work and energy); (2) Most approaches are limited to damage detection (Level I) and localization (Level II) only; (3) Finally, most approaches are limited to detecting damage in slender beams (i.e., Euler-Bernoulli) with relatively low aspect (depth-to-length) ratios. Consequently, there is a need to extend the Level II approaches to Level III and Level IV NDE methodologies for damage evaluation in more complex systems, such as deep beams and stubby beams, whose response are no longer based on the simplified Euler-Bernoulli theory. Although a significant amount of research has been conducted on the analysis and design of deep beams (Rogowsky and MacGregor 1986, Kong 1990, Ashraf 1997, Oh and Shin 2001, Park and Daniel 2007), a relatively limited research effort has been devoted for damage prediction beyond structures modeled as Euler-Bernoulli (i.e., slender) beams (Swamidas *et al*. 2004, Dansheng *et al*. 2007, Karve *et al*. 2011).

This paper presents a Level III damage evaluation methodology, which simultaneously, identifies the location, the extent, and the severity of stiffness damage in deep beams. Kong *et al*. (1990) defined a deep beam as a beam having a depth comparable to the span length. Deep beams are commonly integrated into contemporary structures in the form of foundations, overhangs, and transfer girders, etc. Thus, damage evaluation of deep beams is an imperative activity for public safety officials, since these structural elements may form integral parts of critical structures such as tall buildings, offshore structures, and foundations. Note that no analytical studies on NDE of deep beams have been identified by the authors in literature.

The methodology, to evaluate Level III damage in a structural system, is developed on the bases of the force-displacement relations of the Timoshenko beam theory and the concept of invariant stress resultants across the beam sections. The latter concept states that at any given cross section and under certain restrictive loading conditions, the resultant internal force distribution in a structural member is not affected by the inflicted damage. At that section, damage is modeled using local decreases in the bending and shear stiffnesses of the structural elements. These changes are in turn related to measurable deformational response quantities, such as deflections and rotations. It is shown here that the deformational and kinematic equations of the Timoshenko beam theory in conjunction with the principle of invariant stress resultants can be used to develop a Level III NDE methodology for the evaluation of damage in deep beams.

Previous research efforts showed that despite its relatively simplistic displacement field and stress resultants (where transverse shear strain distribution is assumed to be constant through the beam thickness and therefore requires problem dependent shear correction factors), the Timoshenko beam theory accurately predicts the response of deep beams. For instance, based on the analysis performed on the simply supported thick isotropic beams (Sayyad *et al*. 2011), it was shown that the Timoshenko beam theory yields comparable maximum transverse displacement and fundamental natural frequency to higher order beam theories, where displacement component due to shear deformation is assumed to be parabolic, sinusoidal, hyperbolic or exponential in nature with respect to thickness coordinate. Furthermore, based on the natural frequencies and modes of a cantilever beam, Labuschagne *et al*. (2009) concluded that the Timoshenko theory is close to the two-dimensional elasticity for modes of practical importance even for relatively short beams.

It should be noted that the authors proposed a damage evaluation theory for Timoshenko beams in an earlier work (Dincal and Stubbs 2013). Although the principle of invariant stress resultants was also utilized to establish the theory in the relevant work, the basis for damage evaluation is rather different in this study. Firstly, damage is detected via solving a system of underdetermined linear equations, which are developed based on nodal stiffness values attained prior to and after damage has accrued. Secondly, local decreases in both bending and shear stiffnesses are identified by utilizing vertical displacements and cross-sectional rotations at the centerline of the beam in this study. Lastly, dynamically measured (modal) flexibility matrix is utilized to estimate the deformational response quantities (i.e., pre- and post-damaged rotations and the vertical displacements), which may be more appealing to perform damage evaluation in field. These items are discussed in detail in the sections below.

2. Proposed damage detection theory

2.1 Principle of invariant stress resultants

It can be shown rigorously that the net internal force existing at any cross-section of the beam is not affected by the inflicted damage, provided that the external loadings in the undamaged and damaged beams are identical, and the topological configurations of the two systems are unaltered by the imposed damage. Under the latter scenario, the following conditions hold for the internal bending moment and internal shear force at an arbitrary section x along the length of the beam before and after damage

$$M(x) = M(x)^* \tag{1}$$

$$V(x) = V(x)^* \tag{2}$$

where the asterisks in Eqs. (1) and (2) represent bending moment and shear force distribution in the damaged beam. Here the bending moment and shear force are the invariant stress resultants.

2.2 Summary of the Timoshenko Beam Theory

According to the Timoshenko beam theory, the stress resultants may be expressed in terms of the material and sectional properties, as well as the rotation and the transverse deflection measured at the centerline of a beam (Reddy 1997)

$$M(x) = EI\frac{d\phi}{dx} \tag{3}$$

$$V(x) = GAK_s\left(\phi + \frac{dw}{dx}\right) \tag{4}$$

where the constants E and G denote the modulus of elasticity and shear modulus, respectively, and I represents the moment of inertia of the cross-sectional area A. The term K_S in Eq. (4) is the shear correction factor, which is commonly defined as the ratio of average shear strain to the shear strain at the centroid of the section. The transverse deflection and the rotation of the centroidal axis of the Timoshenko beam are denoted by w and ϕ, respectively, in the above equations. The Timoshenko beam theory relaxes the normality assumption of the Euler-Bernoulli beam theory by including a constant state of transverse shear strain throughout the beam thickness and planes that are normal to the beam axis in the undeformed state, do not necessarily remain normal to the beam axis after deformation (Reddy 1997).

2.3 Damage evaluation approach

Assume that a local damaging event in a beam-type structure may be expressed in terms of a decrease in the bending and shear stiffnesses of its sub-element(s). The problem here is to identify the location of the damaged sub-elements within the beam and quantify the amount of stiffness degradation inflicted in each damaged region. For a beam that is comprised of NE sub-elements and NN nodes (as depicted in Figs. 1 and 2), the pristine and damaged flexural stiffnesses of the j^{th} element may be represented by EI_j and EI_j^*, respectively. Similarly, the pristine and damaged shear stiffnesses of the j^{th} element may be represented by GA_j and GA_j^*, respectively.

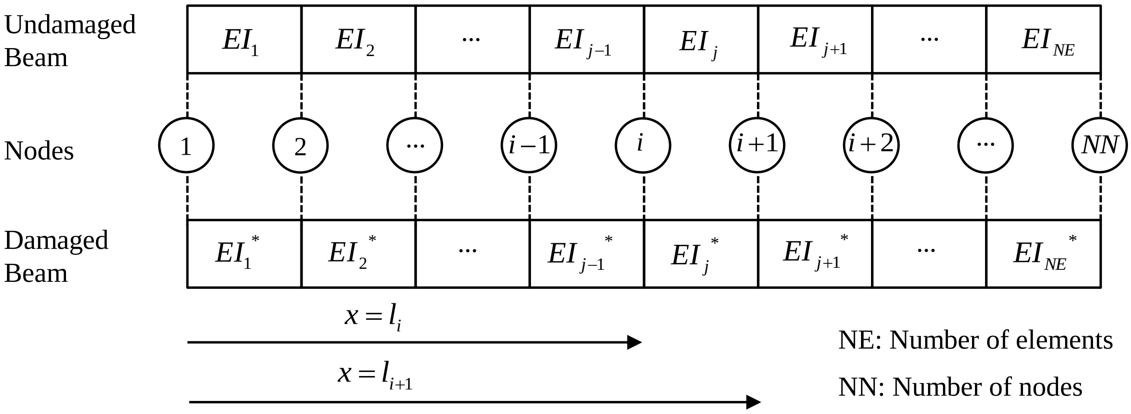

Fig. 1 Damage detection model utilized to predict the changes in flexural stiffness

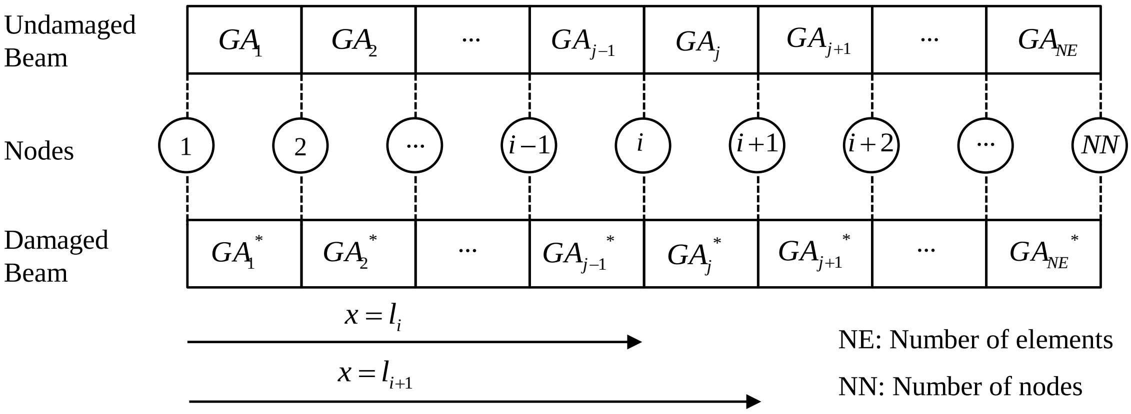

Fig. 2 Damage detection model utilized to predict the changes in shear stiffness

2.3.1 Damage evaluation methodology to predict the changes in flexural stiffness

Using Eq. (1), following condition holds at the i^{th} node of the beam (at $x = l_i$)

$$M(l_i) = M^*(l_i) \tag{5}$$

Utilizing the fundamental relationship between the first derivative of rotation and bending moment, as given by the Timoshenko beam theory in Eq. (3), the above expression can be written as

$$EI_i \frac{d\phi_i}{dx} = EI_i^* \frac{d\phi_i^*}{dx} \tag{6}$$

where EI_i is the flexural stiffness and ϕ_i is the rotation of the centroidal axis at the i^{th} node of the beam. The asterisk represents the same parameters at the damaged beam.

The flexural stiffness at a node can be expressed in terms of the stiffnesses of its neighboring elements by utilizing the Fourier series representation. From calculus, the Fourier series representation of any function converges to a value that is the average of the values immediately to the left and to right of the discontinuity (Kreyszig 1999). Therefore, at $x = l_i$, EI_i converges to

$$EI_i = \frac{1}{2}\left(EI_{j-1} + EI_j\right) \tag{7}$$

Similarly, for the damaged beam

$$EI_i^* = \frac{1}{2}\left(EI_{j-1}^* + EI_j^*\right) \tag{8}$$

Then, from Eq. (6)-(8), it follows that at the i^{th} node

$$\frac{1}{2}\left(EI_{j-1} + EI_j\right)\frac{d\phi_i}{dx} = \frac{1}{2}\left(EI_{j-1}^* + EI_j^*\right)\frac{d\phi_i^*}{dx} \tag{9}$$

Assuming a constant flexural stiffness distribution for the undamaged beam (i.e., for $j = 1..NE, EI_j = EI$) and collecting element stiffnesses on the right hand side of Eq. (9) gives

$$2\frac{d\phi_i}{dx} = \left(\frac{EI_{j-1}^* + EI_j^*}{EI}\right)\frac{d\phi_i^*}{dx} \tag{10}$$

Simplifying Eq. (10) leads to the following result

$$2\frac{d\phi_i}{dx} = \left(\frac{EI_{j-1}^*}{EI} + \frac{EI_j^*}{EI}\right)\frac{d\phi_i^*}{dx} \tag{11}$$

Defining the damage ratio as

$$\gamma_j^{EI} = \frac{EI_j^*}{EI} \tag{12}$$

Eq. (11) can be expressed as

$$2\frac{d\phi_i}{dx} = \left(\gamma_{j-1}^{EI} + \gamma_j^{EI}\right)\frac{d\phi_i^{\,*}}{dx} \tag{13}$$

Using the recursive scheme established in Eq. (13), the relation between the damage indices for the j^{th} and the $(j+1)^{th}$ beam elements at the $(i+1)^{th}$ node becomes

$$2\frac{d\phi_{i+1}}{dx} = \left(\gamma_j^{EI} + \gamma_{j+1}^{EI}\right)\frac{d\phi_{i+1}^{\,*}}{dx} \tag{14}$$

For a beam with NN nodes and NE sub-elements (where $NE = NN - 1$), $NN - 2$ linear equations can be written using the pattern defined by Eqs. (13) and (14). This process results in a system of underdetermined linear equations. Moore-Penrose pseudo-inverse may then be used to obtain the generalized inverse of the matrix built by re-arranging the system of linear equations. This process yields the unknown element damage indices, each representing the ratio of the damaged flexural stiffness to the undamaged one.

The system of equations for damage evaluation can be written in the form

$$A_{(NN-2)x(NE)}\ \gamma_{(NEx1)}^{EI} = B_{(NN-2)x1} \tag{15}$$

where the $NEx1$ (i.e., NE by 1) vector, γ^{EI}, denotes the flexural damage index vector to be evaluated.

$$\gamma_{(NEx1)}^{EI} = \begin{bmatrix} \cdots \\ \gamma_j^{EI} \\ \gamma_{j+1}^{EI} \\ \cdots \end{bmatrix} \tag{16}$$

The $(NN-2)x(NE)$ matrix A and $(NN-2)x1$ matrix B contain the derivatives of cross sectional rotations of the damaged and undamaged beams, respectively.

$$A_{(NN-2)x(NE)} = \begin{bmatrix} \cdots & \cdots & \cdots & \cdots & \cdots & \cdots & \cdots \\ \cdots & 0 & \frac{d\phi_i^{\,*}}{dx} & \frac{d\phi_i^{\,*}}{dx} & 0 & \cdots & \cdots \\ \cdots & \cdots & 0 & \frac{d\phi_{i+1}^{\,*}}{dx} & \frac{d\phi_{i+1}^{\,*}}{dx} & 0 & \cdots \\ \cdots & \cdots & \cdots & \cdots & \cdots & \cdots & \cdots \end{bmatrix} \tag{17}$$

$$B_{(NN-2)x1} = \begin{bmatrix} \cdots \\ 2\frac{d\phi_i}{dx} \\ 2\frac{d\phi_{i+1}}{dx} \\ \cdots \end{bmatrix} \tag{18}$$

The solution to Eq. (15) is given by

$$\gamma^{EI} = A_P^{-1} B \tag{19}$$

where A_P^{-1} is the pseudo-inverse of A.

The predicted severity of the localized damage can be expressed in terms of the pristine and damaged flexural stiffnesses as

$$\alpha_j^{EI} = \frac{\Delta EI_j}{EI} = \frac{EI_j^* - EI}{EI} = \frac{EI_j^*}{EI} - 1 = \gamma_j^{EI} - 1 \tag{20}$$

2.3.2 Damage evaluation methodology to predict the changes in shear stiffness

Similar expressions can be developed to the ones described above upon utilizing the internal shear force distribution. Using Eq. (2), following condition holds at the i^{th} node of the beam (at $x = l_i$)

$$V(l_i) = V^*(l_i) \tag{21}$$

Utilizing the fundamental relationship given in Eq. (4), the internal shear force distribution can be related to the transverse deflection, the rotation of the centroidal axis, and the material as well as sectional properties of the beam. Then, Eq. (21) may be rewritten as

$$GA_i K_s \left(\phi_i + \frac{dw_i}{dx} \right) = GA_i^* K_s \left(\phi_i^* + \frac{dw_i^*}{dx} \right) \tag{22}$$

where GA_i is the shear stiffness, ϕ_i is the rotation of the centroidal axis, and $\frac{dw_i}{dx}$ is the derivative of the transverse deflection at the i^{th} node of the beam. The asterisk represents the same parameters at the damaged beam.

As before, the shear stiffness at a node can be expressed in terms of the stiffnesses of its neighboring elements by utilizing the Fourier series representation. At $x = l_i$, GA_i converges to

$$GA_i = \frac{1}{2}\left(GA_{j-1} + GA_j\right) \tag{23}$$

Similarly, for the damaged beam

$$GA_i^* = \frac{1}{2}\left(GA_{j-1}^* + GA_j^*\right) \tag{24}$$

Then, from Eq. (22)-24), it follows that at the i^{th} node

$$\frac{1}{2}\left(GA_{j-1} + GA_j\right) K_s \left(\phi_i + \frac{dw_i}{dx} \right) = \frac{1}{2}\left(GA_{j-1}^* + GA_j^*\right) K_s \left(\phi_i^* + \frac{dw_i^*}{dx} \right) \tag{25}$$

Assuming a constant shear stiffness distribution for the undamaged beam (i.e., for $j =$

$1..NE, GA_j = GA$), eliminating the shear correction factor K_s, and collecting element stiffnesses on the right hand side of Eq. (25) leads to

$$2\left(\phi_i + \frac{dw_i}{dx}\right) = \left(\frac{GA_{j-1}{}^{*} + GA_j{}^{*}}{GA}\right)\left(\phi_i{}^{*} + \frac{dw_i{}^{*}}{dx}\right) \tag{26}$$

Simplifying Eq. (26) leads to the following result

$$2\left(\phi_i + \frac{dw_i}{dx}\right) = \left(\frac{GA_{j-1}{}^{*}}{GA} + \frac{GA_j{}^{*}}{GA}\right)\left(\phi_i{}^{*} + \frac{dw_i{}^{*}}{dx}\right) \tag{27}$$

Expressing the damage ratio as

$$\gamma_j^{GA} = \frac{GA_j{}^{*}}{GA} \tag{28}$$

Eq. (27) can be written as

$$2\left(\phi_i + \frac{dw_i}{dx}\right) = \left(\gamma_{j-1}^{GA} + \gamma_j^{GA}\right)\left(\phi_i{}^{*} + \frac{dw_i{}^{*}}{dx}\right) \tag{29}$$

Using the recursive scheme established in Eq. (29), the relation between the damage indices for the j^{th} and the $(j+1)^{th}$ beam elements at the $(i+1)^{th}$ node becomes

$$2\left(\phi_{i+1} + \frac{dw_{i+1}}{dx}\right) = \left(\gamma_j^{GA} + \gamma_{j+1}^{GA}\right)\left(\phi_{i+1}{}^{*} + \frac{dw_{i+1}{}^{*}}{dx}\right) \tag{30}$$

As before, a beam with NN nodes and NE sub-elements (where $NE = NN - 1$), $NN - 2$ linear equations can be written using the pattern defined by Eqs. (29) and (30). Moore-Penrose pseudo-inverse may then be used to obtain the generalized inverse of the matrix built upon re-arranging this system of linear equations. This process yields the unknown element damage indices, each representing the ratio of the damaged shear stiffness to the undamaged one.

The system of equations can be written in the form

$$C_{(NN-2)x(NE)}\,\gamma_{(NEx1)}^{GA} = D_{(NN-2)x1} \tag{31}$$

where the $NEx1$ (i.e., NE by 1) vector, γ^{GA}, denotes the shear damage index vector to be evaluated.

$$\gamma_{(NEx1)}^{GA} = \begin{bmatrix} \cdots \\ \gamma_j^{GA} \\ \gamma_{j+1}^{GA} \\ \cdots \end{bmatrix} \tag{32}$$

The $(NN-2)x(NE)$ matrix C and $(NN-2)x1$ matrix D contain the sum of the rotation of the centroidal axis and the first derivative of the transverse deflection of the damaged and undamaged beams, respectively.

$$C_{(NN-2)x(NE)} = \begin{bmatrix} \cdots & \cdots & \cdots & \cdots & \cdots & \cdots & \cdots \\ \cdots & 0 & \left(\phi_i^* + \dfrac{dw_i^*}{dx}\right) & \left(\phi_i^* + \dfrac{dw_i^*}{dx}\right) & 0 & \cdots & \cdots \\ \cdots & \cdots & 0 & \left(\phi_{i+1}^* + \dfrac{dw_{i+1}^*}{dx}\right) & \left(\phi_{i+1}^* + \dfrac{dw_{i+1}^*}{dx}\right) & 0 & \cdots \\ \cdots & \cdots & \cdots & \cdots & \cdots & \cdots & \cdots \end{bmatrix} \tag{33}$$

$$D_{(NN-2)x1} = \begin{bmatrix} \cdots \\ 2\left(\phi_i + \dfrac{dw_i}{dx}\right) \\ 2\left(\phi_{i+1} + \dfrac{dw_{i+1}}{dx}\right) \\ \cdots \end{bmatrix} \tag{34}$$

The solution to Eq. (31) is given by

$$\gamma^{GA} = C_P^{-1} D \tag{35}$$

where C_P^{-1} is the pseudo-inverse of C.

The predicted severity of the localized damage can be expressed in terms of the pristine and damaged shear stiffnesses as

$$\alpha_j^{GA} = \frac{\Delta GA_j}{GA} = \frac{GA_j^* - GA}{GA} = \frac{GA_j^*}{GA} - 1 = \gamma_j^{GA} - 1 \tag{36}$$

3. Numerical verification of the proposed methodology

A set of numerical experiments are utilized to validate the proposed methodology. These numerical experiments are intended to substitute the more costly experimental studies by using two-dimensional finite element simulations of deep beams.

3.1 Description of the test beam

A length to depth ratio of two is considered here to model the deep beam. The identified test structure is a cantilever beam of rectangular cross-section, which is made of 2.5 in. (6.35 cm.) thick solid steel. The depth and the length of the test beam are 30 in. (76.2 cm.) and 60 in. (152.4 cm.), respectively. Fig. 3 depicts the elevation and cross-sectional views of the test beam. Table 1 lists the material and sectional properties of the beam.

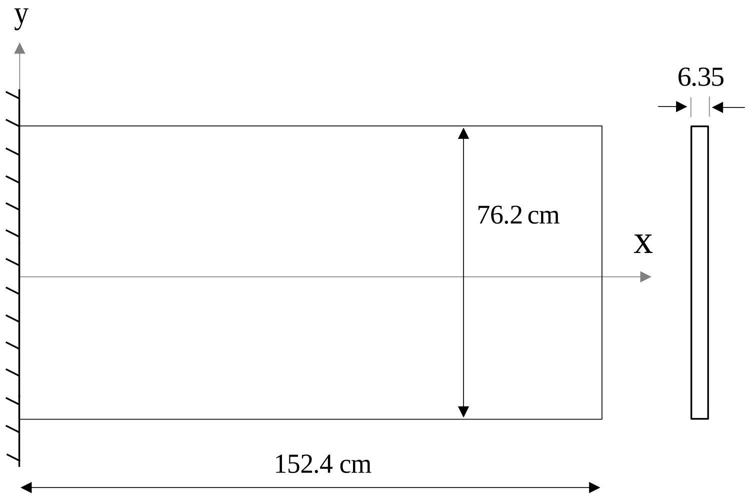

Fig. 3 Schematic of the test beam

Table 1 Material and section properties of the test beam

Description	Magnitude
Span Length (cm)	152.4
Beam Thickness (cm)	6.35
Beam Depth (cm)	76.2
Cross-sectional Area (cm2)	483.9
Moment of Inertia (cm4)	234130.2
Mass Density (kg/m3)	7850
Modulus of Elasticity (N/m2)	$20\text{x}10^{10}$
Poisson’s ratio	0.30

A comparison of the transverse deflections along the centerline of the beam obtained by the Euler-Bernoulli beam theory, the Timoshenko beam theory and two-dimensional elasticity solution is provided here to demonstrate how accurately the Timoshenko beam theory predicts the response of the specified deep beam. Fig. 4 depicts the ratio of vertical displacement to the span length of the beam when the free end is subjected to a static load of 133.5 kN (30 kips). As can be seen, the exact solution obtained via the theory of elasticity is fairly close to the one obtained via the Timoshenko beam theory, whereas the Euler-Bernoulli beam fails to represent the deformational characteristics of the test beam. For comparison purposes, the vertical displacement to span length ratios at the free end of the beam are $2.745\text{x}10^{-4}$, $2.637\text{x}10^{-4}$, and $2.207\text{x}10^{-4}$ for the two-dimensional elasticity, the Timoshenko beam theory, and the Euler-Bernoulli beam theory, respectively. The error between the elasticity and Timoshenko beam solutions is only 3.9% whereas; the Euler-Bernoulli beam theory yields a 19.6% error.

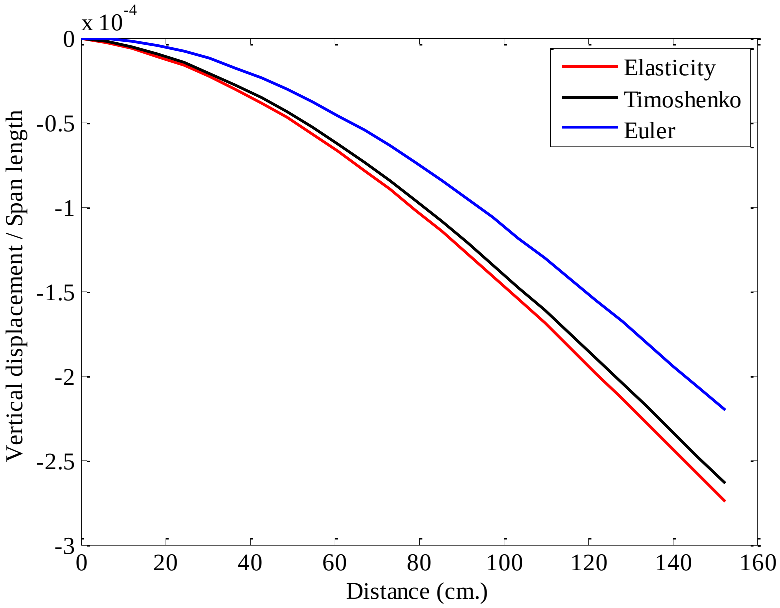

Fig. 4 Vertical displacement of the deep beam normalized by span length

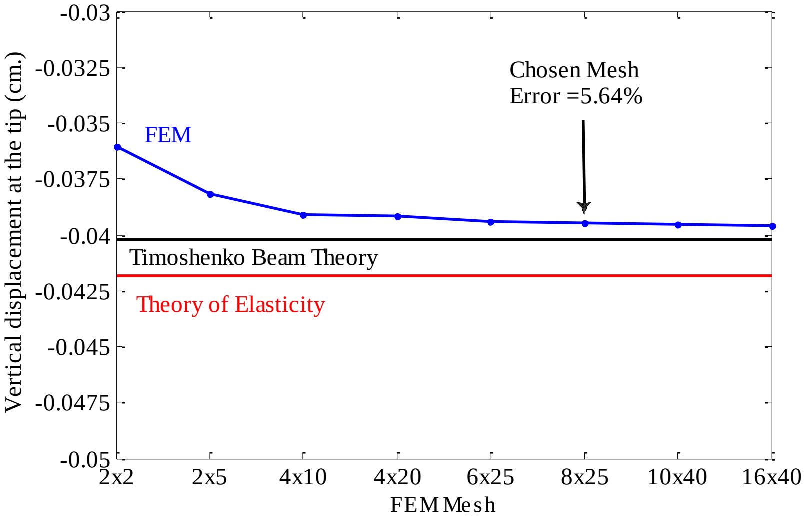

Fig. 5 Convergence of the FEM compared with the solution from the Theory of Elasticity and the Timoshenko Beam Theory

Numerical experiments are based on the finite element (FE) model of the beam, which is constructed using bilinear quadrilateral plane elements. Therefore, convergence tests are performed to choose an appropriate finite element mesh that can provide an accurate prediction of the deformation of the beam. To accomplish the latter end, the vertical displacement at the tip of the

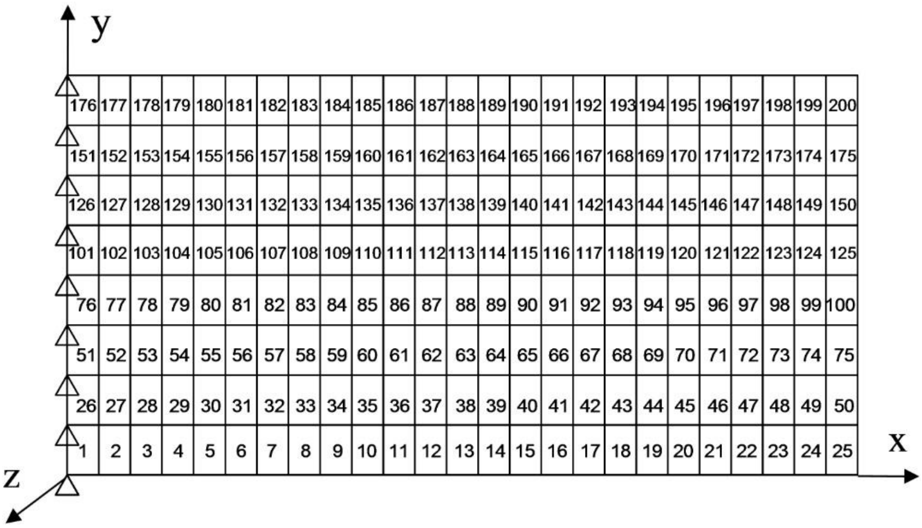

Fig. 6 Finite element mesh of the deep beam

cantilever beam is compared to the solutions given by the theory of elasticity and the Timoshenko beam theory. As before, the free end is subjected to a static load of 133.5 kN (30 kips). Utilizing eight different mesh sizes of progressively decreasing coarseness (see Fig. 5), it is concluded that the predictions of the FE model converge to the numerical solutions given by the Timoshenko Beam Theory (Reddy 1997) and the Theory of Elasticity (Ugural and Fenster 2003) when the mesh is designated by 8x25. In this model, the difference between the numerical solution and the solution obtained from the Theory of Elasticity is 0.0236 mm, which corresponds to an error of 5.6%. Likewise, the difference between the numerical solution and the solution obtained from the Timoshenko Beam Theory is 0.0072 mm, which corresponds to an error of 1.8%.

The chosen finite element mesh of the test beam contains 200 plane elements. A typical quadrilateral element is 2.4 in. (6.1 cm.) wide, 3.75 in. (9.53 cm.) deep, and 2.5 in. (6.35 cm.) thick in the perpendicular z direction. Fig. 6 depicts the selected finite element mesh of the beam. The plane stress assumption is adopted in the FE solution.

3.2 Proposed damage scenarios

Three different parameters are varied to generate different damage cases: the damage location, the damage extent, and the damage severity. The damage location corresponds to the center of the inflicted damage. The extent of damage is represented by the area of the damaged region. Finally, the damage severity is defined as the percent reduction in the material properties of individual plane elements within an area defined by the damage extent. Young's modulus and/or Poisson's ratio are reduced to simulate damage in this study. Note that, reducing the elastic modulus solely has been the common practice so far in numerical studies available in literature. Since any alteration in the material properties of a structure in real life may also involve a change Poisson's ratio, here, it is deemed appropriate to simulate damage by adjusting the Poisson's ratio in addition to elastic modulus in the FEM of the test structure as well. The proposed damage scenarios are summarized below.

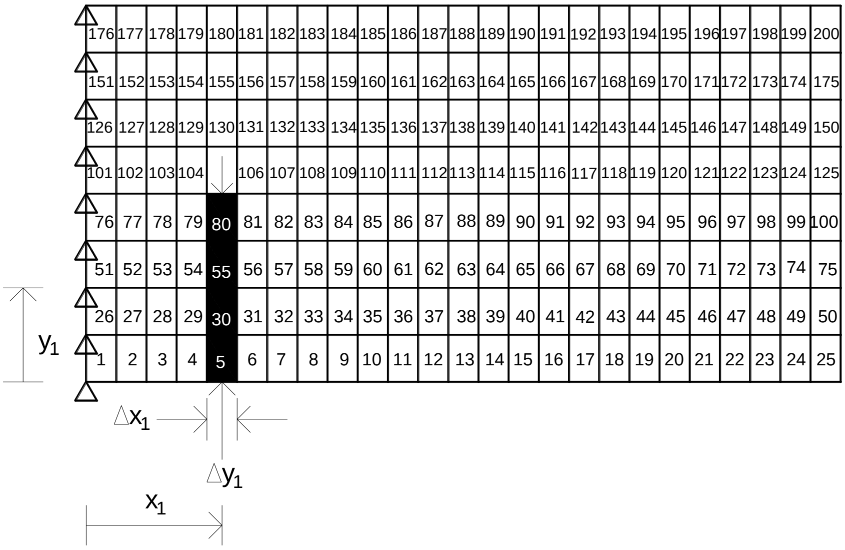

Fig. 7 Schematic representation of Damage Scenario 1

3.2.1 Damage scenario 1

This damage scenario is intended to simulate stiffness degradation at a single location that is centered at 27.4 cm. from the clamped end and at 19.1 cm. from the bottom of the beam. The extent of damage is 6.1 cm. wide and 38.1 cm. deep, which corresponds to 2.0% of the beam's total surface area. Elastic moduli of plane elements 5, 30, 55, and 80 are decreased by 10% to simulate the prescribed damage scenario. The darkened region in Fig. 7 depicts the first damage scenario on the simulated beam. Table 2 summarizes the geometric and elastic details of the damage.

3.2.2 Damage scenario 2

This damage scenario represents a case containing multiple damage locations. Damage is simulated by reducing the elastic modulus and Poisson's ratio of the plane elements located at the damaged region. Fig. 8 shows the schematic of the second damage scenario on the simulated beam. Table 3 summarizes the geometric and elastic details of the damage.

Table 2 Geometric and elastic details of Damage Scenario 1

Damage Location		Damage Size			Damage	Damaged
x (cm.)	y (cm.)	Δx (cm.)	Δy (cm.)	ΔA (cm^2)	Severity	Elements
27.4	19.1	6.1	38.1	232.4	-10% of E	5, 30, 55, 80

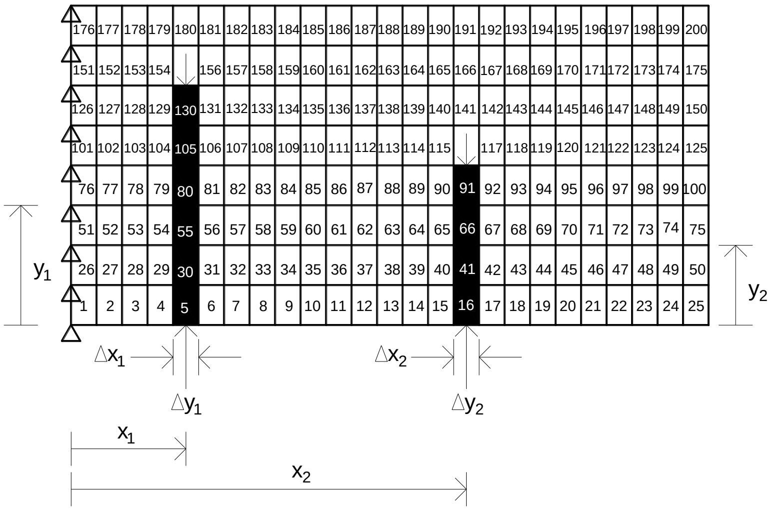

Fig. 8 Schematic representation of Damage Scenario 2

Table 3 Geometric and elastic details of Damage Scenario 2

Damage Location		Damage Size			Damage	Damaged
x (cm.)	y (cm.)	Δx (cm.)	Δy (cm.)	ΔA (cm^2)	Severity	Elements
27.4	28.6	6.1	57.2	348.9	-10% of E	5, 30, 55, 80, 105, 130
27.4	28.6	6.1	57.2	348.9	-8% of ν	5, 30, 55, 80, 105, 130
94.5	19.1	6.1	38.1	232.4	-5% of E	16, 41, 66, 91
94.5	19.1	6.1	38.1	232.4	-7% of ν	16, 41, 66, 91

3.3 Proposed experimental arrangement

The proposed NDE methodology utilizes the rotations and the vertical displacements of the pristine and damaged beams. Although an infinite number of data points are available in theory, only a limited number of sensors can be used to collect data in practice. In order to simulate this more realistic case, sensor layout given in Fig. 9 is proposed. Response data are collected from the numerical experiments at these given sensor locations.

Note that, two-dimensional plane elements were utilized to build the finite element models of the test beam. These plane elements contain horizontal and vertical degree of freedoms only. Thus, while the vertical displacements are readily available at the given sensor locations, the cross-sectional rotations must be approximated by using the horizontal DOFs of the plane quadrilaterals. Consider the schematic given in Fig. 10, which represents a fraction of a deflected shape of the beam.

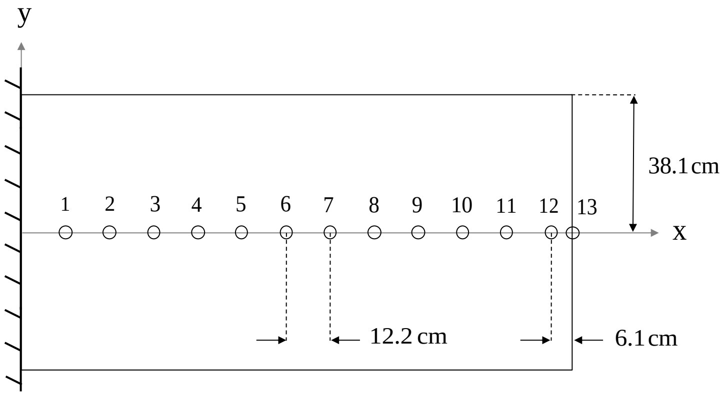

Fig. 9 Sensor layout for the test beam

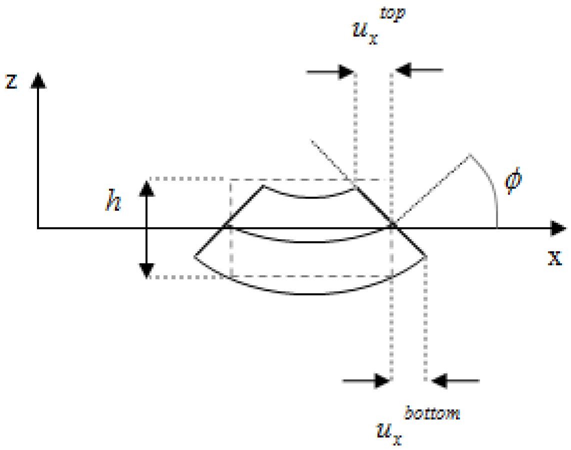

Fig. 10 Fraction of a deflected shape of the beam

The rotation at the centerline of the beam may be approximated by

$$\phi = \frac{u_x^{top} - u_x^{bottom}}{h} \tag{37}$$

where u_x^{top} and u_x^{bottom} represent the outermost top and bottom horizontal nodal displacements on the finite element mesh of the beam. The vertical distance between u_x^{top} and u_x^{bottom} is denoted by h which corresponds to the depth of the beam. Eq. (37) replicates the outputs of the rotary sensors depicted in Fig. 9. Note that, Fig. 10 is not intended to represent an actual schematic of the deflected shape; it is only provided for visualization purposes. Also, note that Eq. (37) is solely proposed to estimate the cross-sectional rotations required by the NDE methodology, which are unavailable in the finite element model due to the use of plane quadrilateral elements.

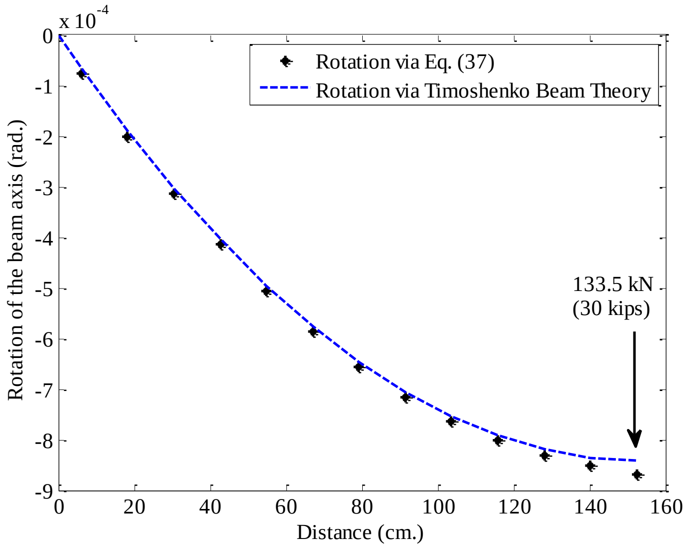

Fig. 11 Comparison of beam rotational profiles obtained via Eq. (37) and the Timoshenko Beam Theory

To provide a comparison on the accuracy of the approximation scheme given in Eq. (37), rotational profile computed using the Timoshenko Beam Theory is compared to the one obtained from the finite element model at the centerline of the beam via Eq. (37) (see Fig. (11)). As before, the free end of the beam is subjected to a static load of 133.5 kN (30 kips). The error is as low as 3.2% at the free end, which indicates that Eq. (37) adequately represents the rotational profile at the centerline of the beam.

3.4 Basic measurements required by theory

As stated previously, the fundamental assumption behind the theory presented in this paper is that the internal stress resultants at a given section of the beam (i.e., bending moments and shear forces in this case) are not affected by the inflicted damage. This may be achieved in two ways: (1) Application of identical static loads prior and subsequent to damage, and; (2) Utilizing dynamically measured (modal) flexibility matrix to estimate the pre- and post-damage rotations and the vertical displacements.

The flexibility matrix is the inverse of the stiffness matrix and relates the applied static loads to the resulting structural deformations. Each row of the flexibility matrix may be interpreted as the deformed shape of a structure due to a unit load applied at the corresponding DOF. It has been shown that the dynamically measured or modal flexibility matrix can be accurately created using few of the lower vibration modes Berman and Flannely (1971). This observation makes the modal flexibility particularly attractive since modal data are mostly limited to the first few mode shapes and eigenfrequencies in practical applications. Considering the applicability of the proposed methodology to real time health monitoring, it may be more practical to use dynamic data in lieu of static deformations. It should be noted that the constant external load required for invariant stress resultants are automatically satisfied when using this approach.

If all modes are measured, the flexibility matrix may be written as (Kim 2002)

$$K^{-1} = F = \sum_{i=1}^{r=p} \frac{1}{\lambda_i m_i} \phi_i \phi_i^T \tag{38}$$

where the pxp matrix represents the full size flexibility matrix and m_i, ϕ_i, and λ_i denote the ith modal mass, mode shape, and eigenvalue, respectively.

Upon expressing the jth component of the ith modal vector by ϕ_{ji}, the deflection profile due to a unit load applied at the jth DOF (denoted here by the vector u_j) may be written as (Kim 2002)

$$u_j = \sum_{i=1}^{r} \frac{\phi_{ji}}{\lambda_i m_i} \phi_i \tag{39}$$

It should be noted that Eq. (39) represents an approximate deflection profile if only r modes (where $r << p$) are measured. However, few lower modes should be sufficient to provide an accurate representation of the system response due to the significant contributions of the lower modes (as the ith eigenvalue increases substantially for higher modes) to the flexibility matrix.

A more generalized form of the above equation may be formulated by including rotational DOFs to the modal flexibility matrix. In this case, vector u_j may also represent the rotation of a structure if rotational degrees of freedom are utilized in computing Eq. (39). A certain drawback of the dynamically measured flexibility is the uncertainty in modal mass. Either mass-normalized mode shapes or the modal mass itself is necessary to accurately construct the modal flexibility matrix. Therefore, an extension to the numerical scheme proposed by Kim (2002) is used here to approximate the modal mass, as it may not be available in real-time health monitoring.

If the density, cross-sectional area and moment of inertia of a beam-like structure are known, and translational and rotational modal amplitudes are measured, then the ith modal mass, m_i, may be approximated by

$$m_i = \int_0^L \rho A u_i(x) u_i(x) dx + \int_0^L \rho I \varphi_i(x) \varphi_i(x) dx \tag{40}$$

where ρ, A, I and L are the density, the cross-sectional area, the moment of inertia and the span length of the beam, respectively. The functions $u_i(x)$ and $\varphi_i(x)$ denote the translational and rotational profiles of the ith bending mode. Note that, the above algebraic process summarized in Eqs. (38)-(40) is not a part of the damage evaluation methodology proposed in this study. They are merely provided to show the method's applicability in field conditions where static deformations under similar loading conditions prior to and subsequent to damage may be difficult to achieve. Numerical studies given in this manuscript utilizes modal data in lieu of static deformations to detect and quantify damage.

The following procedure may be employed to perform a Level III damage evaluation with the proposed methodology.

1. Define the damage detection model (DDM). The DDM is a simplified mechanical model of a structure, which is used to determine the approximate location and severity of damage in the true

structure.

2. Obtain the pre-damage and post-damage modal parameters. These parameters include natural frequencies and translational as well as rotational modal amplitudes at available sensor locations. Note that as stated above, for the numerical experiments performed in this study, nodal rotations at given sensor locations were approximated by using the outermost top and bottom horizontal nodal displacements on the finite element mesh of the beam (see Eq. (37)). In practice, translational and angular accelerometers may be used to measure the motions dictated by the NDE theory.

3. Use the numerical scheme given in Eq. (40) to approximate the modal mass using the modal parameters obtained in the previous step. It is recommended to use cubic spline interpolation with uniform intervals to generate a finer sensor layout along the length of the beam. This step is necessary to achieve good displacement and rotation profiles from coarse and/or uneven measurement spacing.

4. Compute the pre-damage and post-damage modal flexibilities and define the common loading condition (e.g., the same column or row of the flexibility matrix in pre- and post-damage state). These quantities represent vertical displacements and cross-sectional rotations at the centerline of the beam.

5. Employ central difference approximation to calculate the first derivative of the cross-sectional rotation and vertical displacement. As before, use cubic spline interpolation with uniform intervals to generate a finer sensor layout along the length of the beam prior to applying central difference approximation. Create the systems of linear equations given in Eqs. (15) and (31) and solve for the unknown damage ratios, which provide the change in bending and shear stiffnesses due to damage, respectively.

3.5 Damage prediction results for the case studies

The number of degrees of freedom for the modal flexibility is 26 (13 translations and 13 rotations). The vertical displacements and cross-sectional rotations are estimated by the 25th and 26th modal flexibilities, respectively. These represent deformations measured at the centerline of the cantilever test beam due to a unit load (1 kip or 4448.2 N) applied at the free end. Fig. 12 depicts the vertical displacements and rotations of the undamaged beam approximated in this manner using the first two bending modes only. Also provided in Fig. 12 for comparison purposes is the deflected shape of the beam due the static unit load applied at the free end. Note the accuracy of the approximation although modal data are only limited to the first two mode shapes and eigenfrequencies. Cubic spline interpolation with 0.3 in. (0.762 cm.) uniform intervals is used to generate a finer sensor layout along the length the beam. Interpolation leads to 201 nodal points including the node that corresponds to the clamped support. It should be noted that the given interpolation interval (and therefore 201 total pseudo nodal points) is by no means a “required” or “pre-determined” number compulsory for successful damage evaluation.

For convenience, damage localization results are reported using the reciprocal of the proposed damage indicators, γ_j^{EI} and γ_j^{GA}. Then, the following relationships hold

$$\beta_j^{EI} = \frac{1}{\gamma_j^{EI}} \tag{41}$$

$$\beta_j^{GA} = \frac{1}{\gamma_j^{GA}} \tag{42}$$

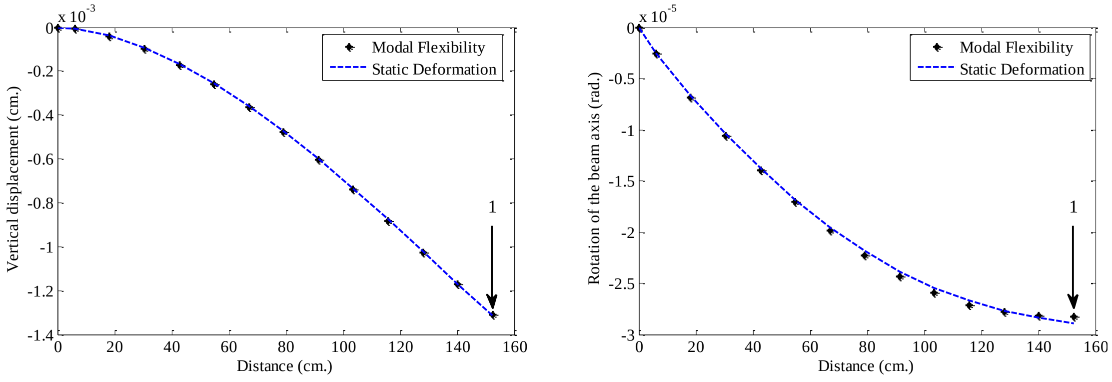

(a) (b)

Fig. 12 Comparison of static vertical displacements (a) and rotations (b) to the ones approximated by modal flexibility

The updated indices, represented by β_j^{EI} and β_j^{GA}, are greater than unity in regions where stiffness degradation has occurred.

3.5.1 Damage scenario 1

The damage detection result using the damage location indicator β_j^{EI} (Eq. (41)) is depicted in Fig. 13. Table 4 summarizes the method's damage localization accuracy. Note that L_P and L_T denote the axial length (Δx) of the predicted and true damage extents along the x-coordinate, respectively. The term $L_T \subset L_P$ shows whether the predicted damage extent (L_P) contains the true damage extent (L_T). For instance, $L_T \subset L_P = 100\%$ indicates that the predicted region covers 100% of the simulated (true) damage region. The damage severity and the damage extent are estimated after enhancing the sensor resolution along the predicted damage location at the damaged structure only, since a more detailed analysis of the damage requires a finer measurement grid along the location of the flaw. Here, the enhanced sensor resolution corresponds to the nodes of the finite element mesh at the centerline of the beam. The predicted damage severity is computed using Eq. (20). Fig. 14 depicts the estimated damage severity and damage extent. Table 5 displays the assessment of damage extent and damage severity accuracy. Fig. 15 and Fig. 16 show the damage prediction results for Damage Scenario 1 using the damage indicator β_j^{GA}. Damage is localized using Eq. (42) and quantified using Eq. (36) after improving the sensor resolution at the predicted damage location. Tables 6 and 7 summarize the performance of the NDE methodology, which utilizes β_j^{GA} for evaluating damage.

Table 4 Assessment of the damage localization accuracy for Damage Scenario 1 using β_j^{EI}

Damage Central Location (cm.)		Error (%)	$L_T \subset L_P$
True	Predicted		
27.4	24.9	1.6	100%

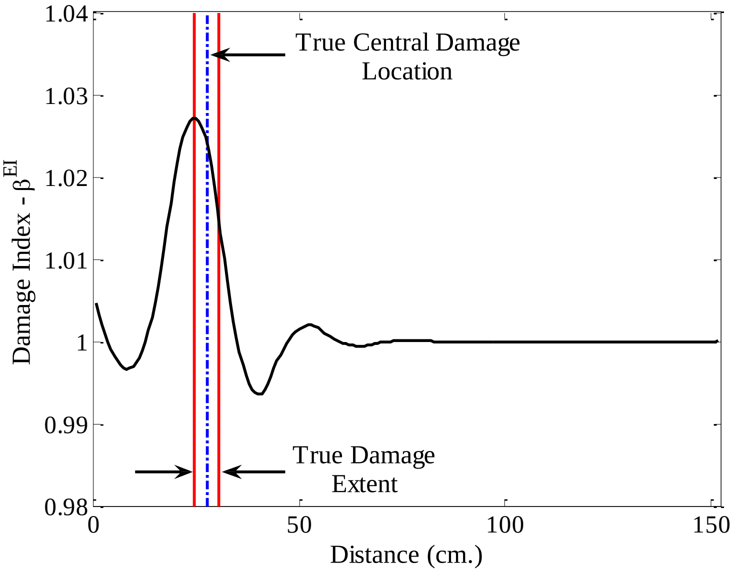

Fig. 13 Damage localization result for Damage Scenario 1 using β_j^{EI}

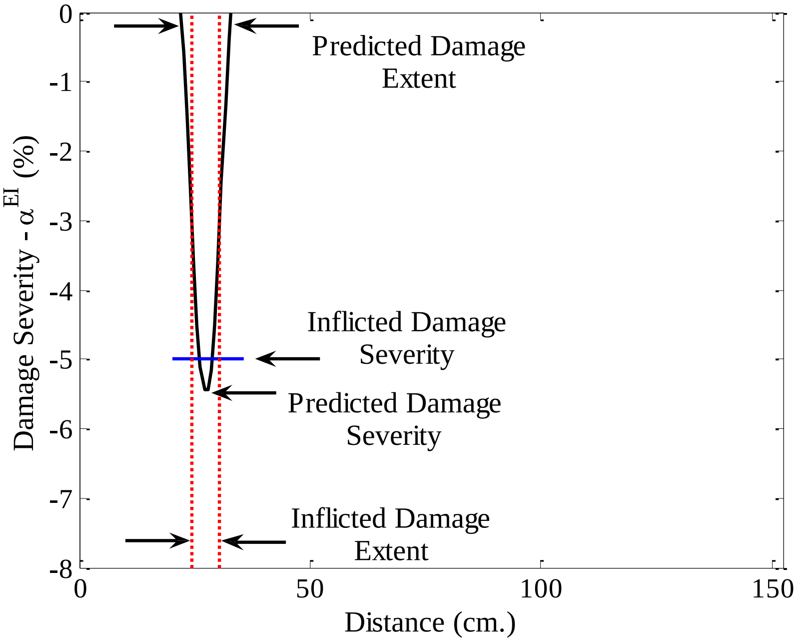

Fig. 14 Damage extent and severity estimate for Damage Scenario 1 using α_j^{EI}

Table 5 Assessment of the damage extent and severity accuracy for Damage Scenario 1 α_j^{EI}

Damage Extent (cm.)		Error (%)	Damage Severity (%)		Error (%)
True	Predicted		True	Predicted	
6.1	11.4	-3.5	-5.0	-5.5	0.5

Table 6 Assessment of the damage localization accuracy for Damage Scenario 1 using β_j^{GA}

Damage Central Location (cm.)		Error (%)	$L_T \subset L_P$
True	Predicted		
N/A	FP	100.0	0%
27.4	23.4	2.6	100%

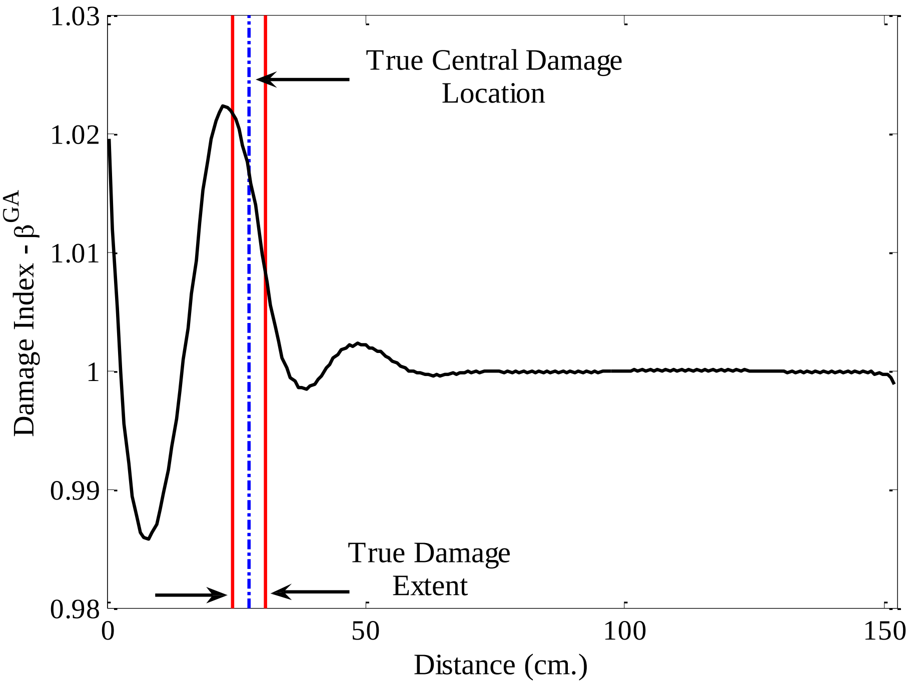

Fig. 15 Damage localization result for Damage Scenario 1 using β_j^{GA}

Table 7 Assessment of the damage extent and severity accuracy for Damage Scenario 1 using α_j^{GA}

Damage Extent (cm.)		Error (%)	Damage Severity (%)		Error (%)
True	Predicted		True	Predicted	
N/A	FP	100.0	N/A	FP	100.0
6.1	10.7	-3.0	-5.0	-7.8	2.8

3.5.2 Damage scenario 2

Figs. 17 and 18 depict the damage prediction results for Damage Scenario 2 using the damage indicator β_j^{EI}. Tables 8 and 9 summarize the performance of the damage evaluation methodology for the damage scenario.

Table 8 Assessment of the damage localization accuracy for Damage Scenario 2 using β_j^{EI}

Damage Central Location (cm.)		Error (%)	$L_T \subset L_P$
True	Predicted		
27.4	24.9	1.6	100%
94.5	98.0	-2.3	100%

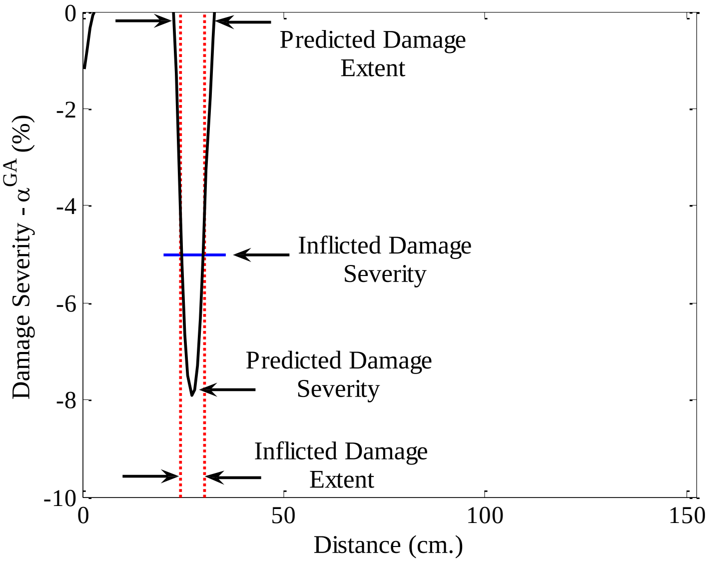

Fig. 16 Damage extent and severity estimate for Damage Scenario 1 using α_j^{GA}

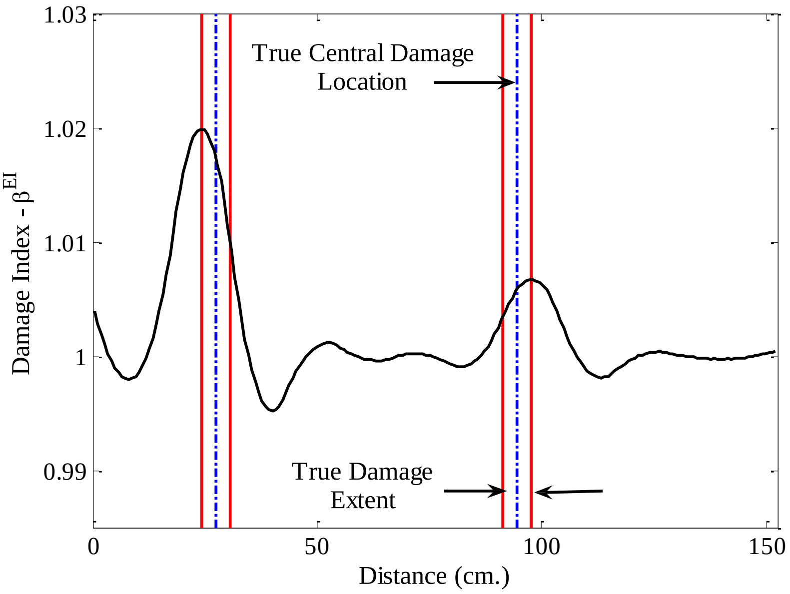

Fig. 17 Damage localization result for Damage Scenario 2 using β_j^{EI}

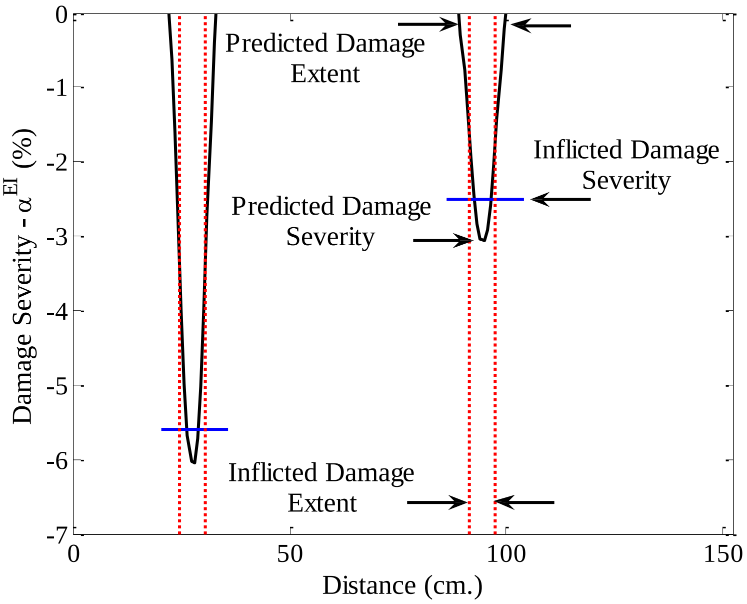

Fig. 18 Damage extent and severity estimate for Damage Scenario 2 using α_j^{EI}

Table 9 Assessment of the damage extent and severity accuracy for Damage Scenario 2 using α_j^{EI}

Damage Extent (cm.)		Error (%)	Damage Severity (%)		Error (%)
True	Predicted		True	Predicted	
6.1	11.4	-3.5	-5.6	-6.0	0.4
6.1	11.4	-3.5	-2.5	-3.1	0.6

Figs. 19 and 20 depict the damage prediction results for Damage Scenario 2 using the damage indicator β_j^{GA}. Tables 10 and 11 summarize the performance of the damage evaluation methodology for the damage scenario.

Table 10 Assessment of the damage localization accuracy for Damage Scenario 2 using β_j^{GA}

Damage Central Location (cm.)		Error (%)	$L_T \subset L_P$
True	Predicted		
N/A	FP	100.0	0%
27.4	23.4	2.6	100%
94.5	96.5	-1.3	100%

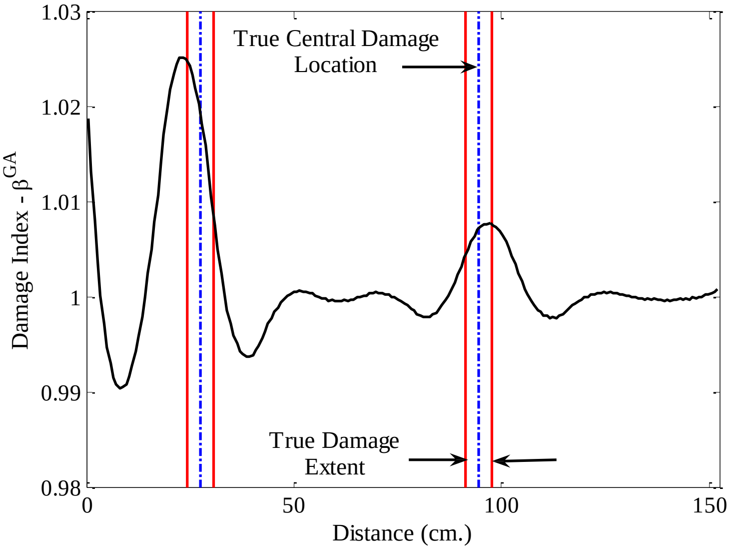

Fig. 19 Damage localization result for Damage Scenario 2 using β_j^{GA}

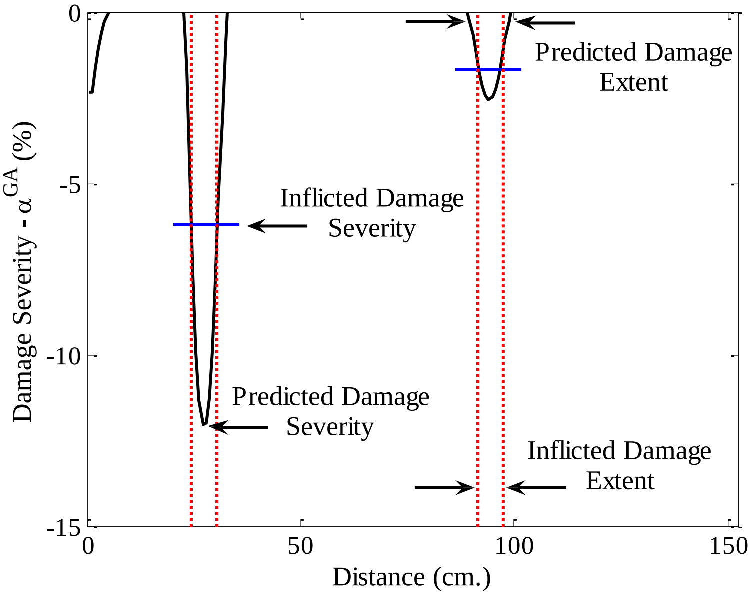

Fig. 20 Damage extent and severity estimate for Damage Scenario 2 using α_j^{GA}

Table 11 Assessment of the damage localization accuracy for Damage Scenario 2 using α_j^{GA}

Damage Extent (cm.)		Error (%)	Damage Severity (%)		Error (%)
True	Predicted		True	Predicted	
N/A	FP	100.0	N/A	FP	100.0
6.1	9.9	-2.5	-6.2	-12.0	5.8
6.1	10.7	-3.0	-1.7	-3.1	1.4

3.6 Discussion of results

The performance of the proposed damage detection methodology was based on accurately identifying three damage-related parameters: the location of damage, the extent of damage, and the severity of damage. The proposed methodology is limited to one-dimensional Timoshenko Beam Theory. Therefore, possible damage locations were only identified along the longitudinal axis of the beam; here, the distribution of damage along the beam depth is not addressed.

Damage localization accuracy was quantified in terms of a dimensionless position error, which can be obtained by dividing the distance between the true and predicted damage locations to the total length of the beam. This error was expressed in terms of percentage as

$$e_L = \frac{x_T - x_P}{L} \times 100 \tag{43}$$

where x_T and x_P correspond to the true and predicted damage locations and L is the total length of the beam. The predicted damage location, x_P, in Eq. (43) corresponds to the peak value of the damage indicator, β_j^{EI} (Eq. (41)) or β_j^{GA} (Eq. (42)), within the vicinity of the dominating peaks in damage localization charts. On reviewing the damage prediction results obtained using the damage location indicator β_j^{EI}, the largest error between the central location of the true and the predicted damage, e_L, was 2.3% in Damage Scenario 2. Excluding the false negative prediction (i.e., the true damage location is not predicted) in the vicinity of the clamped support in Damage Scenarios 1 and 2, the largest damage localization error using β_j^{GA} was 2.6%. These false predictions may be due to the boundary conditions utilized in finite element model of the beam.

Note that, the support conditions of model do not precisely match the ones utilized in the theoretical solution.

Damage extent accuracy was initially quantified using the subset notation. For instance, if the predicted damage extent contained the true damage extent, then $(L_T \subset L_P) = 1.0$. Here, L_P denotes the axial length of the predicted damage region where the damage indicator β_j^{EI} or β_j^{GA}, is greater than one. The true damage extent, L_T, corresponds to the total length of the damage region along the x-coordinate (Δx). Damage extent was subsequently quantified by enhancing the sensor resolution in region of the predicted damage location. In this study, the enhanced sensor resolution corresponds to the nodes of the finite element mesh at the centerline of the beam. It should be noted that the damage locations are unambiguous in almost all damage scenarios even without refining the sensor layout. Mounting additional sensors on the damaged structure will improve the damage severity and extent estimates; however are not mandatory for successful damage localization.

The damage extent can be expressed as the footprint of damage severity. Therefore, the extent of damage corresponded to the axial length of the region where the predicted damage severity (i.e., α_j^{EI} or α_j^{GA}) was less than zero. Once a numerical estimate for the damage extent was available, damage extent accuracy was quantified by dividing the difference between the length of the true and predicted damaged regions to the total length of the beam. This error may be expressed in terms of a percentage as

$$e_E = \frac{L_T - L_P}{L} \times 100 \tag{44}$$

where L_T refers to the true length of the inflicted damage (Δx) and L_P represents the length of the predicted damaged region. L is a metric, which denotes the total length of the beam. The largest error between the true and the predicted damage extent, e_E, was 3.5% using the damage severity indicator α_j^{EI} and 3.0% using α_j^{GA} (excluding the false predictions).

The error in damage severity estimation was quantified by utilizing the fractional error in stiffness prediction. Utilizing the true and predicted flexural stiffnesses of the j^{th} element (k_{jT} and k_{jP}, respectively), and the undamaged flexural beam stiffness (k), the error in stiffness prediction can be expressed in terms of a percentage as

$$e_K = \frac{k_{jT} - k_{jP}}{k} \times 100 \tag{45}$$

Utilizing the true and predicted damage severities, Eq. (45) can be rewritten as

$$e_K = \frac{k(1+\alpha_{jT}) - k(1+\alpha_{jP})}{k} \times 100 \tag{46}$$

where α_{jT} and α_{jP} correspond to the true and predicted damage severities of the j^{th} beam element, respectively. The above expression finally simplifies to Eq. (47), which was utilized to compute the error in damage severity estimation.

$$e_K = (\alpha_{jT} - \alpha_{jP}) \times 100 \tag{47}$$

The predicted damage severity in Eq. (47) corresponds to the peak value of damage severity computed directly using Eq. (20) for α_j^{EI} or Eq. (36) for α_j^{GA}. Note that, the damage severities were quantified after improving the sensor resolution in region of the predicted damage locations.

The damaged regions previously identified with the proposed sensor layout in Fig. 9 were instrumented subsequently to predict the severity of damage. Also, note that the true damage severity, denoted by α_{jT} in Eq. (47), may not correspond to the actual reduction imposed on the modulus of elasticity of the beam elements. For example, in Damage Scenario 1 where the elastic moduli of the four of the eight plane elements centered at 27.4 cm. from the clamped end and centered at 19.1 cm. from the bottom of the beam were reduced by 10%, does not manifest a 10% stiffness reduction in the one-dimensional beam. For this reason, equivalent one-dimensional flexural and shear stiffnesses for the damaged and the undamaged beam were estimated from the two-dimensional damage scenarios as described below. Stiffnesses of the individual plane elements located along the depth of the beam were utilized in order to achieve this end.

Suppose that a system of linear springs connected in parallel (as given in Fig. 22) models the plane elements located at an arbitrary distance x_0 from the clamped end (see Fig. 21).

The equivalent bending stiffness of the linear springs model, for the j^{th} location, given in Fig. 22 can then be written as

$$k_{j\ equ}^{EI} = k_{BN}(h_N)^2 + k_{Bi}(h_i)^2 + \ldots + k_{Ai}(h_i)^2 + k_{AN}(h_N)^2 \tag{48}$$

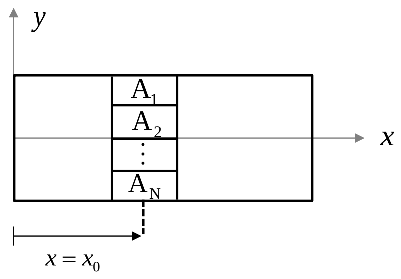

Fig. 21 Plane elements centered at the distance x_o

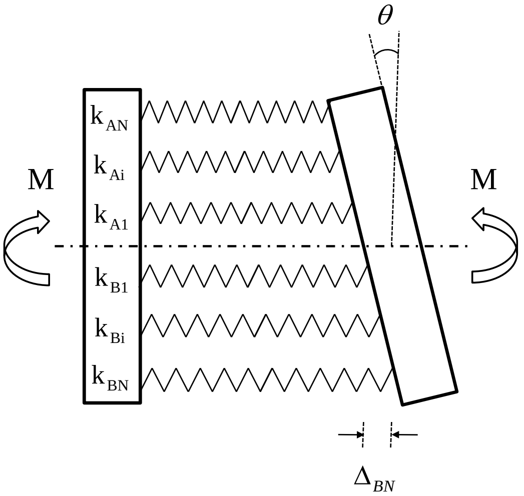

Fig. 22 The deformed shape of the linear springs model subjected to bending

where h_i represents the height of the i^{th} spring measured from the neutral axis. The subscripts A and B represent the springs located above and below the neutral axis, respectively. The stiffness of each spring that appears in Eq. (48) can be estimated from the following equation

$$k_i = \frac{E_i A_i}{l_i} \tag{49}$$

where the terms E, A and l denote the elastic modulus, the area, and the length of the individual plane elements, respectively.

An equivalent bending stiffness expression similar to the one given in Eq. (48) can be written for the damaged structure (denoted by, ${k_j^{EI}}_{equ}^{*}$, where the moduli of elasticity of one or more plane elements are reduced) as well. Then, the true equivalent one-dimensional flexural stiffness damage severity, α_{jT}^{EI}, can be computed as

$$\alpha_{jT}^{EI} = \frac{{k_j^{EI}}_{equ}^{*}}{{k_j^{EI}}_{equ}} - 1 \tag{50}$$

Similarly, the system of linear springs depicted in Fig. 23 may be used to derive an equivalent shear stiffness from the shear stiffnesses of the individual plane elements located at an arbitrary distance x_0 from the clamped end (see Fig. 21).

The equivalent shear stiffness of the linear springs model given in Fig. 23 can be written as

$$ {k_j^{GA}}_{equ} = k_{BN} + k_{Bi} + \ldots + k_{Ai} + k_{AN} \tag{51}$$

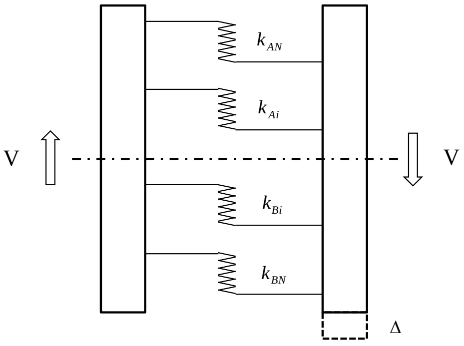

Fig. 23 The deformed shape of the linear springs model under the applied shear force

The stiffness of each spring that appears in the above equation can be estimated from the following

$$k_i = \frac{G_i A_i}{l_i} \tag{52}$$

where G, A and l denote the shear modulus, the area, and the length of the individual plane elements, respectively. As before, similar expressions can be written to obtain the equivalent shear stiffness for the damaged structure. Note that, the fundamental relationship between the modulus of elasticity (E) and Poisson's ratio (ν) is utilized to compute the shear modulus of each plane element, which are represented by a linear spring in Eq. (52). Therefore, changes imposed on the Poisson's ratio due to damage reveal themselves as changes in the shear modulus as shown in Eq. (53)

$$G^* = \frac{E^*}{2(1+\nu^*)} \tag{53}$$

where the asterisks represent the damaged material properties.

Finally, using Eq. (51)-(53) the true equivalent one-dimensional shear stiffness damage severity, α_{jT}^{GA}, can be computed as

$$\alpha_{jT}^{GA} = \frac{k_{j\ equ}^{GA\ *}}{k_{j\ equ}^{GA}} - 1 \tag{54}$$

On reviewing the damage prediction results obtained using the damage severity indicator α_j^{EI}, the largest error between the true flexural stiffness damage severity and the predicted flexural stiffness damage severity was 0.6% in Damage Scenario 2. Excluding the false negative prediction in the vicinity of the clamped end, using the damage indicator α_j^{GA}, the largest error between the true shear stiffness damage severity and the predicted shear stiffness damage severity was 5.8% in Damage Scenario 2.

4. Conclusions

A Level III damage evaluation methodology, which simultaneously, identifies the location, the extent, and the severity of damage in deep beams was proposed in this paper. The proposed methodology was developed on the bases of the force-displacement relations of the Timoshenko beam theory and the concept of invariant stress resultants before and after damage. It is concluded that structural damage in deep beams can accurately be localized and quantified with the given procedure. The performance of the proposed damage evaluation technique was evaluated using the response data collected from a set of numerical experiments, which were based on a finite element model of a deep cantilever beam. Pre-damage and post-damage modal flexibilities were used to obtain vertical displacements and rotations required by the theory. Damage was simulated by modifying Young's modulus and/or Poisson's ratio of individual plane elements located within the domain of the damage extent. Changes in the flexural and shear stiffnesses due to damage were investigated with the proposed methodology. The damage indicator γ^{EI} gives the ratio of the flexural stiffnesses before and after damage. Damage was successfully localized and quantified using γ^{EI}. The damage indicator γ^{GA} gives the ratio of the shear stiffnesses before and after damage. Excluding the false positive predictions at the vicinity of the clamped support, γ^{GA} gave satisfactory damage localization results and damage extent estimates. The predicted damage severities were less satisfactory compared to the ones obtained using γ^{EI}. Damage evaluation in more complex structures, such as deep beams and stubby beams, whose response are no longer based on the simplified Euler-Bernoulli theory is achievable with the proposed methodology.

Acknowledgments

Professor Norris Stubbs passed away on August 9, 2014 prior to seeing this manuscript published. He was an inspiration to many of us with his wisdom, intelligence and integrity. The corresponding author was privileged to have gotten to know and work with him. May God bless his soul.

References

Ashraf, FA. (1997), "Tests of reinforced concrete continuous deep beams", *ACI Struct. J.*, **94**(1), 3-12.

Berman, A. and Flannely, W.G. (1971), "Theory of incomplete models of dynamic structures", *AIAA J.*, **9**(8), 1481-1487.

Cawley, P. and Adams, R.D. (1997), "The locations of defects in structures from measurements of natural frequencies", *J. Strain Anal.*, **14**(2), 49-57.

Choi, S., Park, S. and Stubbs, N. (2005), "Nondestructive damage detection in structures using changes in compliance", *Int. J. Solids Struct.*, **42**(15), 4494-4513.

Choi, S., Sooyong. P., Yoon, S. and Stubbs, N. (2005), "Nondestructive damage identification in plate structures using changes in modal compliance", *NDT & E Int.*, **38**(7), 529-540.

Dansheng, W., Hongping, Z., Chuanyao, C. and Yong, X. (2007), "An impedance analysis for crack detection in the Timoshenko beam based on the anti-resonance technique", *Acta Mechanica Solida, Sinica*, **20**(3), 228-235.

Dincal, S. and Stubbs, N. (2013), "Damage evaluation of Timoshenko beams using invariant stress resultants", *Eng. Struct.*, **56**, 2052-2064.

Hjelmstad, K.D. and Shin, S. (1996), "Crack identification in a cantilever beam from modal response", *J. Sound Vib.*, **198**(5), 527-545.

Karve, P.M., Na, S.W. and Kang, J.W. (2011), "The inverse medium problem for Timoshenko beams and frames: Damage detection and profile construction in the time-domain", *Comput. Mech.*, **47**(2), 117-136.

Kim, B.H. (2002), "Local damage detection using modal flexibility", Ph.D. Dissertation, Texas A&M University, College Station, Texas.

Kim, J.T. and Stubbs, N. (2002), "Improved damage identification method based on modal information", *J. Sound Vib.*, **252**(2), 223-238.

Kim, J.T. and Stubbs, N. (2003), "Crack detection in beam-type structures using frequency data", *J. Sound Vib.*, **259**(1), 145-160.

Kim, J.T. and Stubbs, N. (2003), "Nondestructive crack detection algorithm for full-scale bridges", *J. Struct. Eng. - ASCE*, **129**(10), 1358-1366.

Kong, F.K. (1990), *Reinforced concrete deep beams*, Blackie and Son Ltd, Glasgow, Scotland.

Kreyszig, E. (1999), "Advanced engineering mathematics", 8th Ed., Wiley, New York.

Labuschagne, A., Rensburg, N.F.J. and Merwe, A.J. (2009), "Comparison of linear beam theories", *Math. Comput. Modell.*, **49**, 20-30.

Lifshitz, J.M. and Rotem, A. (1969), "Determination of reinforcement unbonding of composites by a vibration technique", *J. Compos. Mater.*, **3**(3), 412-423.

Oh, J.K. and Shin, S.W. (2001), "Shear strength of reinforced high-strength concrete deep beams", *ACI Struct. J.*, **98**(2), 164-173.

Pandey, A.K. and Biswas, M. (1994), "Damage detection in structures using changes in flexibility", *J. Sound Vib.*, **169**(1), 3-17.

Pandey, A.K., Biswas, M. and Samman, M.M. (1991), "Damage detection from changes in curvature mode shapes" *J. Sound Vib.*, **145**(2), 321-332.

Park, J.W. and Daniel, K. (2007), "Strut-and-tie model analysis for strength prediction of deep beams", *ACI Struct. J.*, **104**(6), 657-666.

Reddy, J.N. (1997) "On locking-free shear deformable beam finite elements", *Comput. Method. Appl. M.*, **149**, 113-132.

Rogowsky, D.M. and MacGregor, J.G. (1986), "Design of reinforced concrete deep beams", *Concrete Int.* , **8**(8), 49-58.

Rytter, A. (1993), "Vibrational based inspection of civil engineering structures", Ph.D. Dissertation, University of Aalborg., Denmark.

Sayyad, A.S. (2011), "Comparison of various refined beam theories for bending and free vibration analysis of thick beams", *Appl. Comput. Mech.*, **5**, 217-230.

Stubbs, N., Kim, J.T. and Topole, K. (1992), "An efficient and robust algorithm for damage localization in offshore platforms", *Proceedings of the 10th ASCE Structures Congress*, San Antonio, Texas., April.

Swamidas, S.J., Yang, X. and Seshadri, R. (2004), "Identification of cracking in beam structures using Timoshenko and Euler formulations", *J. Eng. Mech. -ASCE*, **130**(11), 1297-1308.

Ugural, A.C. and Fenster, S.K. (2003), "Advanced strength and applied elasticity", 4th Ed., Prentice Hall, New Jersey.

Zhang, Z. and Aktan, A.E. (1995) "The damage indices for constructed facilities", *Proceedings of the 13th International Modal Analysis Conference*, Nashville, Tennessee, February.

Zimmerman, D.C. and Kaouk, M. (1994), "Structural damage detection using minimum rank update theory", *J. Vib. Acoust.*, **116**(2), 222-231.

JK